J. Fluid Mech. (2020), *vol*. 900, A17. © The Author(s), 2020.
Published by Cambridge University Press
doi:10.1017/jfm.2020.511

Oblique impact of microspheres on the surface of quiescent liquid

Bingqiang Ji[1], Qiang Song[1,†], Kai Shi[1], Jiaheng Liu[1] and Qiang Yao[1]

[1]Key Laboratory of Thermal Science and Power Engineering of Ministry of Education, Department of Energy and Power Engineering, Tsinghua University, Beijing 100084, PR China

(Received 16 November 2018; revised 21 April 2020; accepted 20 June 2020)

Impact of microspheres on liquid surfaces is a universal phenomenon in nature and in industrial processes. However, most relevant studies have mainly focused on the sphere's vertical impact. Herein, we present the first observation on the oblique impact of microspheres on the surface of quiescent liquid using high-speed microphotography. The sphere motion and liquid surface distortion after the oblique impact are basically different from those after a vertical impact. The sphere rotates and its trajectory deviates from the impact direction during the oblique impact process, while the non-axisymmetric liquid surface distortion experiences an evolution from half-cavity to full-cavity patterns. The dependence of motions of the sphere and the three-phase contact line on the impact angle α and Weber number are investigated, and the scaling laws for the sphere's penetration time and penetration depth are given. We provide a phase diagram with respect to the Weber number and impact angle that describes the observed impact modes of submergence and oscillation, which shows that the critical Weber number between two impact modes increases when the impact angle decreases. Additionally, a scaling model is established based on energy balance to distinguish different impact modes. The model indicates that the critical Weber number for the microsphere's oblique impact is equal to $1/\sin\alpha$ times that for vertical impact, agreeing well with the experimental results.

Key words: contact lines, capillary waves

1. Introduction

Impact of objects on liquid surfaces is ubiquitous in nature and occurs frequently in many industrial processes, e.g. locomotion of insects on water (Hu, Chan & Bush 2003; Bush & Hu 2006), water entry of bullets or bombs (Johnson 1998; Hrubes 2001), capture of particulate matter by wet deposition or wet scrubbing (Jaworek *et al.* 2006; Bae, Jung & Kim 2010), mineral flotation (Mitra *et al.* 2015) and injection metallurgy (Kaptay 1996). Objects interact with the liquid and gas–liquid interface after impact, and may sink into the liquid (Aristoff *et al.* 2010; Liu, He & Evans 2010), oscillate and finally float on the liquid surface (Ji, Song & Yao 2018), or rebound and escape the liquid surface (Lee & Kim 2008). The three-phase contact line (TPCL) may slide (Kim *et al.* 2017) or may be pinned (Ding *et al.* 2015) at the objects' surface, and the fluids may exhibit many complex phenomena of interest, such as cavities (Bergmann *et al.* 2009), ripples (Grumstrup, Keller

† Email address for correspondence: qsong@tsinghua.edu.cn

& Belmonte 2007), splashes (Duez *et al.* 2007) and liquid jets (Gekle *et al.* 2009). Thus, impact of objects on the liquid surface is a multiphase-coupled, sophisticated, physical process, with a broad range of applications (Seddon & Moatamedi 2006; Truscott, Epps & Belden 2013).

The vertical impact of spheres on liquid surfaces has been of primary interest in relevant studies, and this process is determined by the dimensionless parameters of the Weber number We $(= \rho_l u_0^2 d_p/\sigma)$, the Reynolds number Re $(= \rho_l u_0 d_p/\mu_l)$, the Bond number Bo $(= \rho_l d_p^2 g/\sigma)$, the density ratio of the sphere to the liquid D $(= \rho_s/\rho_l)$ and the contact angle θ, where ρ_l, μ_l and σ, denote the density, viscosity and surface tension coefficient of the liquid, u_0 is the impact velocity, d_p and ρ_s are the diameter and density of the sphere, respectively, and g is the gravitational acceleration. Owing to the limit of the research method, the size of the impacting spheres is mainly of the order of millimetres or larger, with a corresponding Bo larger than 10^{-1}. Furthermore, their impact behaviours are dominated by surface tension, hydrodynamic forces, gravity and buoyancy. The experiment on the impact of superhydrophobic millimetre-sized spheres on liquid surfaces by Lee & Kim (2008) observed three impact modes, namely, oscillation, rebound and submergence, with the increase in We. Subsequently, Chen *et al.* (2018) numerically investigated the effect of wettability on the impact behaviour of millimetre-sized spheres and proposed a criterion to distinguish different impact modes. Spheres with a large We and D will sink uniformly after impact the liquid surface owing to their large inertia (Aristoff & Bush 2009), while spheres with a small We or D experience a deceleration process after impact (Aristoff *et al.* 2010), which means that the sphere dynamics and fluid dynamics are coupled. When We increases, the gas–liquid interface will exhibit different cavity types after impact (Aristoff & Bush 2009; Speirs *et al.* 2019). The distortion of the liquid surface after impact is mild and can be considered as quasi-static when We is small, while a deeper cavity is produced owing to the pinning of the TPCL, and liquid splashing may occur above the undisturbed liquid surface during the impact process with a large We. For the microspheres, which are common in many industrial processes, the effect of gravity on the sphere's motion and gas–liquid interface evolution can be neglected completely since $Bo \ll 1$, making them exhibit different impact behaviours compared with millimetre-sized spheres. Wang *et al.* (2017) observed two impact modes of submergence and oscillation in the experiment of microspheres impact liquid surfaces with $We \sim O(10^1)$. Accordingly, our prior simulation research (Ji, Song & Yao 2017) reproduced the submerging and oscillating processes of the microspheres' vertical impact accurately. The characteristics of sphere motion and gas–liquid interface evolution at different stages were illustrated, and it was found that the hydrodynamic force and surface tension dominated the initial and late stages of the impact, respectively, and the energy conversion mechanism during impact was also revealed.

Objects impact the liquid surface at arbitrary angles in practical situations, but researches on the oblique impact mainly focused on the high-speed impact of objects with large sizes. Objects may acquire an upward component of the hydrodynamic force owing to the non-axisymmetric wetting along their velocity direction, which is powerful enough to rebound the objects from the liquid surface. The theoretical research by Johnson & Reid (1975) showed that the impact angle needed for the sphere to rebound should be less than $18^\circ/D^{1/2}$. Clanet, Hersen & Bocquet (2004) and Rosellini *et al.* (2005) investigated the phenomenon of stone skipping, and outlined the scope of impact angle and velocity for the successful rebound of stone. The experimental research by Bodily (2013) found that after a slender cylinder impacted the liquid surface obliquely, a torque was produced owing to the pressure and gravity with different action points and directions, which led

to the rotation of the cylinder and altered the cylinder's trajectory. Correspondingly, the rotation and trajectory offset became larger when the impact angle decreased. Because the impact *We* was relatively small for microspheres, the impact angle would also affect the surface tension which dominates the middle and late stages, and may then alter the motion behaviours of the sphere and fluid.

To deepen our understanding of the oblique impact behaviour of microspheres on liquid surfaces, we investigated experimentally in this study the impact of microspheres on liquid surfaces with different impact angles using a high-speed microphotography technique. The sphere motion and the evolution of the gas–liquid interface at different impact modes are observed, and the effect of the impact angle on the penetration time and penetration depth is studied. We also present the impact-mode phase diagram, and propose a scaling model to distinguish different impact modes based on energy balance, which are verified by comparing them with experimental results.

2. Experiment

As shown in figure 1, a bespoke designed particle feeder with agitation and vibration is used to feed individual microspheres. The detailed operating principle was described by Wu (2013). The particle generation rate was adjusted to ensure that the spheres can impact the liquid surface without disturbing each other. Since the microspheres we adopted have a small terminal velocity u_t of 0.20–1.72 m s^{-1} in air, free fall cannot make them impact the liquid surface with a relative high velocity near its sinking threshold. Thus, a self-made impactor (Wang *et al.* 2017) was designed to realize the high velocity impact of microspheres by inertia separation. The spheres are transported out of the feeder by the gas flow and enter the impactor, and then accelerate under the action of high-speed gas flow after passing through the nozzle. The void below the nozzle is half-filled with liquid, and sealed off from the outside except for a hole at the top, which makes the gas inside the void stagnant and undisturbed by the aforementioned high-speed gas flow. The gas from the nozzle flows out of the impactor from the outlets, whereas the spheres deviate from the gas flow and enter the void through the hole owing to their inertia, and then impact the liquid surface. Two optical glasses are embedded on the two sides of the void, and the inner parts of the glasses are treated with a hydrophobic solution (Gtechniq G5 water repellent coating for glass) to make their contact angle approximately equal to 90°, thus minimising the influence of the meniscus near the glasses on acquired photographs. The impact processes are recorded by high-speed microphotography (Phantom V1612 with a Navitar 12X zoom lens system) from one side of the void at a rate of 28 000 frames per second with a resolution of 1280 pixels × 800 pixels, a lens magnification in the range of 4.2–6.8 and backlight illumination by an LED light source (Kaiwei Optical Company: KW–B50F–HW). The sphere's impact angle and velocity (or *We*) can be adjusted by changing the inclination of the impactor and the gas flow rate at the inlet of the particle feeder, respectively.

The experiment used polymethyl methacrylate (PMMA) microspheres (Suzhou Knowledge & Benefit Sphere Tech. Co., Ltd) with a d_p in the range of 80–380 μm, a ρ_s of 1180 kg m^{-3}. Purified water with a ρ_l of 998.2 kg m^{-3}, a μ_l of 0.0010 Pa s, a σ of 0.0728 N m^{-1}, an apparent advancing contact angle θ_a of $115 \pm 7.5°$ and an apparent receding contact angle θ_r of $50 \pm 7.5°$ (Ji *et al.* 2017), and 5 % propanol solution with a ρ_l of 975.6 kg m^{-3}, a μ_l of 0.0016 Pa s, a σ of 0.0305 N m^{-1}, a θ_a of $109 \pm 7.5°$ and a θ_r of $50 \pm 7.5°$ (Won, Chung & Mills 1981) at room temperature and atmospheric pressure are used as the two liquids.

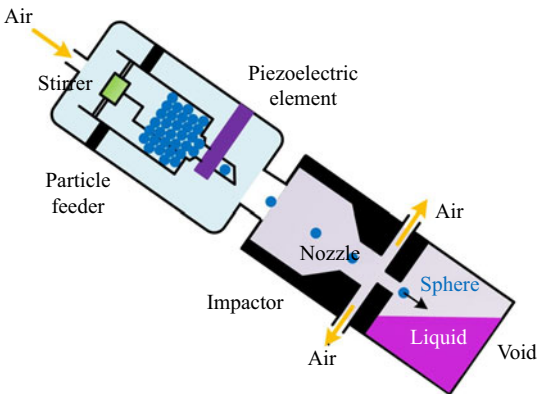

FIGURE 1. Sketch of the experimental set-up.

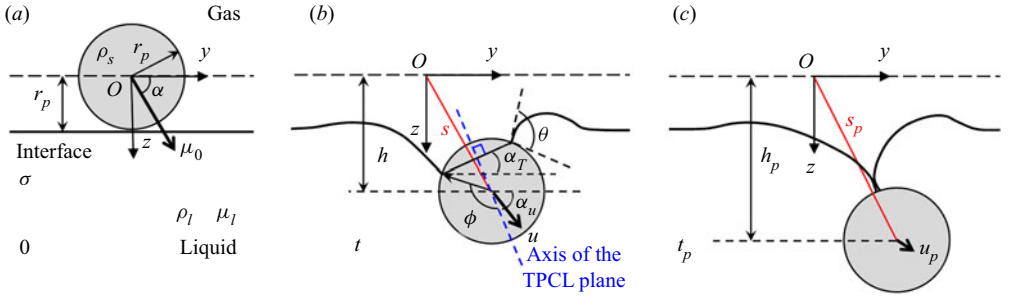

FIGURE 2. Schematic (the symmetric plane) of a microsphere's oblique impact on the liquid surface: (*a*) contact; (*b*) impact; (*c*) submerge.

Figure 2 depicts the oblique impact of a sphere with an impact angle α and a velocity u_0 on the liquid surface, where r_p is the radius of the sphere, s is the sphere displacement, h is the vertical displacement of the sphere, u is the sphere velocity, α_u is the inclination of the sphere velocity vector, and ϕ and α_T are the angular position and inclination of the TPCL, respectively. At the end of the sinking stage (the moment when the liquid surface pinches off for the submergence mode and the moment when the sphere's vertical velocity decreases to zero for the oscillation mode), the sphere has a velocity u_p, a maximum displacement s_p and a penetration depth h_p. The time duration of the sinking stage t_p is referred to as the penetration time. The impacts of 857 individual spheres were analysed with ImageJ and MATLAB 2017a. We measured the sphere diameter, and the positions of sphere and TPCL at each observed time series, and then obtained the impact angle and velocity. The errors of the measurement for the displacement and time were less than or equal to 7 μm and 0.036 ms, respectively. For all of the impact processes in this study, $\alpha = 9.8^\circ$–90°, $We = 1.65$–99.2 and $Re = 115$–1408. Because $Bo \sim 10^{-4}$–$10^{-2} \ll 1$, the effect of gravity can be ignored. Furthermore, because $Re > 10^2$, the viscous effect can also be ignored (Lee & Kim 2008). Additionally, θ and D are fixed in our experiments. Thus, the impact behaviour of the studied spheres can be determined by the two dimensionless parameters of We and α.

3. Results and discussion

3.1. *Typical features of a microsphere's oblique impact*

Two different impact modes, namely the submergence and oscillation, were observed after impact, and the time series of the two typical impact processes representing these two impact modes is shown in figure 3. It is obvious that the sphere motion and liquid surface distortion after an oblique impact are significantly different from those after a vertical impact. The sphere experiences the sinking stage first, where the sphere moves downward and the TPCL slides upward along the sphere surface, and the contact angle θ is basically maintained at θ_a with a little variation. The sinking stage of a submerging sphere can be divided into three stages, including slamming, cavity developing and cavity collapse (Ji *et al.* 2017), and the cavity shape in our study is similar to the quasi-static cavity shape after the steel sphere's impact reported by Aristoff & Bush (2009) and Speirs *et al.* (2019). Because the time duration of the slamming stage is extremely short, the distortion of the liquid surface is small and cannot be observed clearly. During the cavity developing stage, the TPCL on the left-hand side of the sphere first moves below the undisturbed liquid surface compared with the right-hand side, which produces a half-cavity above the sphere's left-hand side (0.10–0.17 ms in figure 3*a*). Subsequently, the TPCL on the right-hand side moves below the undisturbed liquid surface and a non-axisymmetric full-cavity is formed (0.27–0.49 ms in figure 3*a*) with the meniscus curvature in the vertical plane on the right-hand side being larger than that on the left-hand side, while the distortion of the liquid surface after the vertical impact is axisymmetric without any half-cavities. The smaller the impact angle is, the longer the time the half-cavity persists. The cavity collapsing stage arises when the sphere reaches the position where the cavity becomes unstable (0.49 ms in figure 3*a*). Accordingly, the meniscus above the sphere pinches off quickly and the sphere submerges. A bubble is entrapped on the top of the sphere after submergence. It can be concluded from the motion of the bubble that the sphere rotates clockwise (backspin) during the oblique impact process (0.60–0.78 ms in figure 3*a*). An oscillating sphere only experiences the slamming and cavity developing stages during the sinking stage because its vertical velocity decreases to zero before it reaches the position where the cavity becomes unstable. Subsequently, the sphere begins to rise under the action of surface tension, and then enters the reverting stage while the direction of the sphere's horizontal velocity remains unchanged. Correspondingly, the TPCL is pinned on a certain position at the sphere surface with a gradually decreasing θ, while the cavity retracts in the vertical direction (0.79–1.36 ms in figure 3*b*). The small θ_r (or large contact angle hysteresis) of the PMMA sphere results in its not being able to obtain enough kinetic energy at the reverting stage to bounce off the liquid surface (Ji *et al.* 2017). When the sphere is near the horizontal of the undisturbed liquid surface, it moves slowly in the horizontal direction with its vertical motion stopped, and the sphere eventually floats at the liquid surface (1.36–1.82 ms in figure 3*b*). The non-axisymmetry of the cavity decreases gradually at the late stage of the impact. This occurs because of the larger Laplace pressure of the meniscus on the sphere's right-hand side attributed to the larger curvature compared with that on the left-hand side. This effect flattens the meniscus on the right-hand side at a faster rate compared with that on the left-hand side.

3.2. *Motion behaviours of sphere and TPCL*

As mentioned above, α and *We* determine the impact processes in this study, and their effects on the motion behaviours of the sphere and TPCL are discussed in this section.

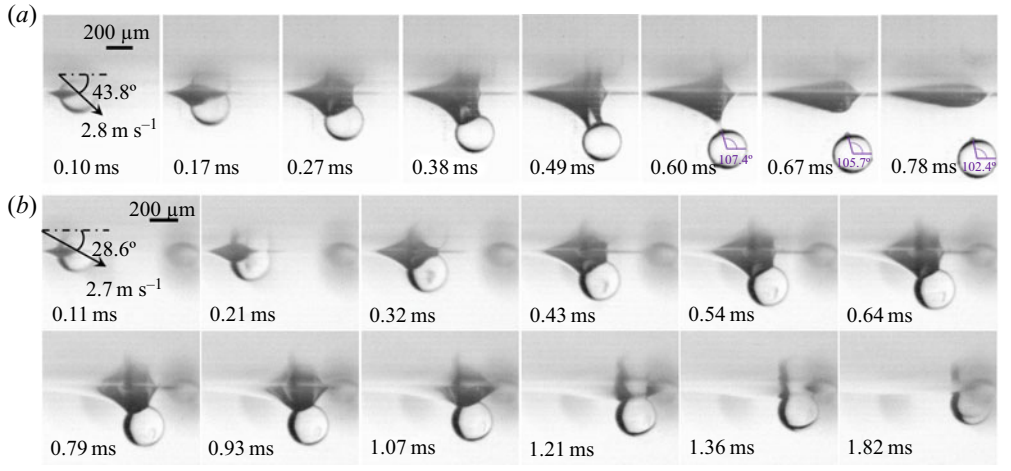

FIGURE 3. Time series of the oblique impact of PMMA microspheres on a water surface exhibiting different impact modes. (*a*) Submergence: $\alpha = 43.8°$, $d_p = 306.0$ μm, $u_t = 1.36$ m s^{-1}, $u_0 = 2.84$ m s^{-1}, $We = 34$ and $Re = 867$. (*b*) Oscillation: $\alpha = 28.6°$, $d_p = 294.3$ μm, $u_t = 1.30$ m s^{-1}, $u_0 = 2.71$ m s^{-1}, $We = 30$ and $Re = 796$.

Figure 4(*a*) shows the trajectories of spheres after impacting on a water surface at different α values when $We = 34$, while the sphere trajectories at different We values when $\alpha = 29.5°$ are shown in figure 4(*b*), whereby the sphere position and time are non-dimensionlized by the characteristic length d_p and time d_p/u_0, respectively. The corresponding sphere velocity (normalized by u_0) evolutions are shown in figure 4(*c*). With the increase in α or We, the impact mode changes from oscillation to submergence. During the sinking stage, the sphere typically moves along its impact direction, with the trajectories deviating downward first and then upward after the early stage of the oblique impact process. The evolutions of sphere velocity at different We or α values show a universal behaviour at the initial stage of impact (slamming stage), and then separate from each other at the late stage of impact, which means that the decay ratios of the sphere's kinetic energy (or momentum) have little difference at the slamming stage. When α decreases, the sphere velocity at the end of the sinking stage u_p decreases, as shown in figure 4(*c*). The decrease in α also makes the sphere's maximum trajectory deviation (Δs_m) during the sinking stage increase, which means that the deviation of the sphere trajectory becomes more obvious, as shown in figure 4(*d*). The decrease in We decreases the sphere velocity at the end of the sinking stage and the maximum deviation of the sphere trajectory (as shown in figure 4*c*,*d*). The velocity of the oscillating sphere at the reverting stage is much smaller than its impact velocity. The vertical motion of the sphere stops, and the sphere slowly slides horizontally at the gas–liquid interface when it rises to the position of $0.8d_p$ below the undisturbed liquid surface.

Figure 3 shows that the TPCL is basically in a plane (TPCL plane). Thus, the angle between the TPCL and the axis of the TPCL plane ϕ (as shown in figure 2*b*) and the inclination of the TPCL plane relative to the horizontal α_T are defined to characterize the wetting ratio of the sphere surface and the position of the TPCL on the sphere surface, and their evolutions with the normalized sphere displacement s/s_p are given in figure 5(*a*,*b*), respectively. For a submerging sphere, ϕ increases rapidly first (slamming stage), and the increase then becomes slower (cavity developing stage), and increases rapidly again to a final value near π (cavity collapsing stage). The evolutions of ϕ with s/s_p have no

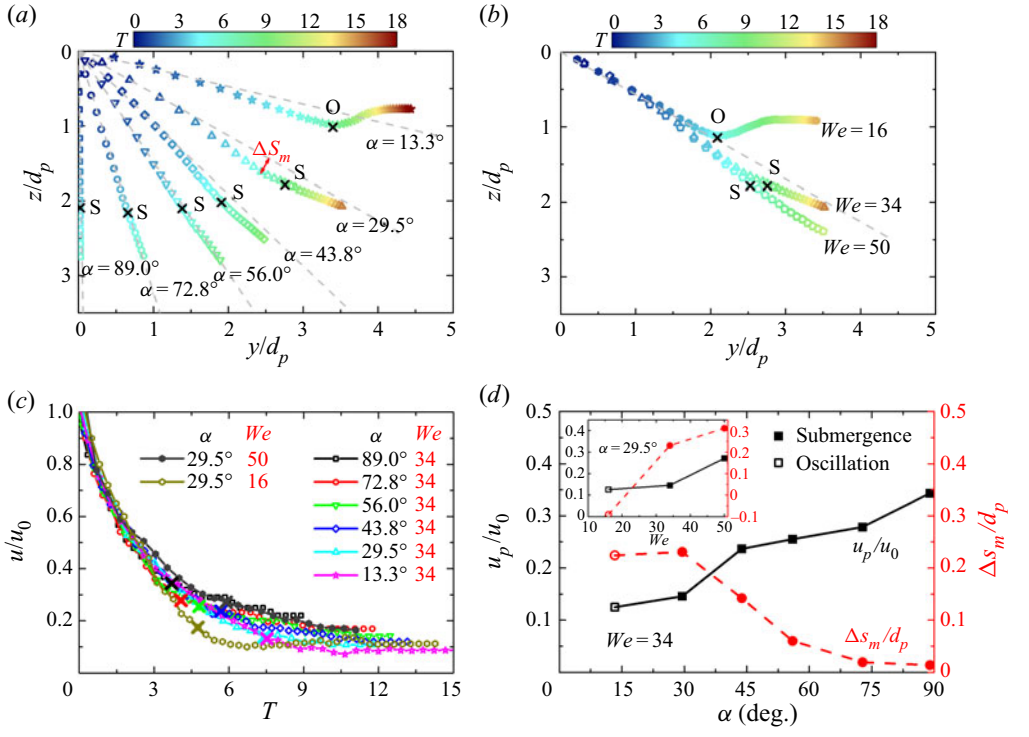

FIGURE 4. Sphere trajectories coloured based on the dimensionless time T ($= tu_0/d_p$) during oblique impact on a water surface: (*a*) $We = 34$ at different α values and (*b*) $\alpha = 29.5°$ at different We values (see supplementary movies 1–8 available at https://doi.org/10.1017/jfm.2020.511). Panel (*c*) is the corresponding sphere velocity evolutions. The grey dashed lines represent the impact directions. The red line with arrows in panel (*a*) represents the sphere's maximum trajectory deviation (Δs_m) during the sinking stage. Here, S and O represent the modes of submergence and oscillation, respectively, while the symbol $\times$ represents the end of the sinking stage. Panel (*d*) is the corresponding sphere velocities at the end of the sinking stage (u_p) and Δs_m as a function of α. The spheres shown in the figure have a u_0/u_t of 1.89–3.70.

obvious difference for submerging spheres at different α and We values. By comparison, ϕ increases more slowly for an oscillating sphere, which is kept almost constant after increasing to a value near $\pi - \theta/2$ at the late cavity developing stage. Accordingly, α_T increases first and then decreases during the sphere's oblique impact process, with a maximum value $< \pi/2 - \alpha_u$, which means that the TPCL plane is not perpendicular to the motion direction and the wetting of the sphere surface is non-axisymmetric along the motion direction; specifically, the wetted part of the sphere surface below the motion axis is larger than that above. When α decreases, the deflection angle of the TPCL plane relative to the equatorial plane (perpendicular to the impact direction) $\pi/2 - \alpha_u - \alpha_T$ increases, which means the non-axisymmetry of sphere wetting increases.

This non-axisymmetric sphere wetting results in the non-axisymmetric pressure (positive at the upstream and negative at the downstream) and shear stress (mainly along the sides) distributions on the sphere surface, significantly influencing the forces acting on the sphere as well as the sphere motion. This non-axisymmetry first makes the hydrodynamic force F_h which dominates the early sinking stage have a downward component F_{hv} perpendicular to the motion direction. Meanwhile, it also generates a

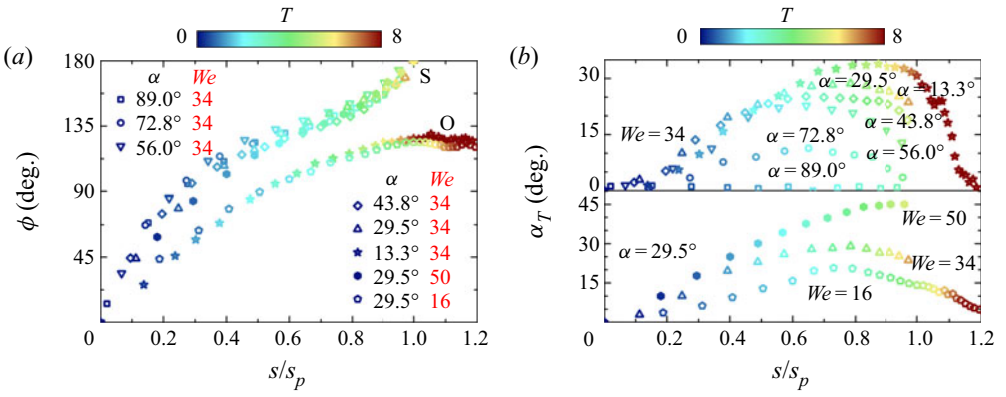

FIGURE 5. Evolutions of (a) the angular position of the TPCL ϕ and (b) the inclination of the TPCL plane α_T as a function of the normalized sphere displacement s/s_p during oblique impact on a water surface, coloured based on the dimensionless time T ($= tu_0/d_p$), where s_p represents the total sphere displacement during the sinking stage.

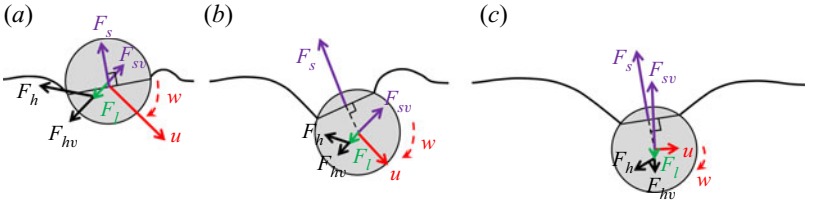

FIGURE 6. Schematics of the forces acting on the microsphere at different stages of the impact process: (a) early sinking stage where the hydrodynamic force F_h dominates, (b) late sinking stage where the surface tension force F_s dominates and (c) reverting stage where the surface tension force F_s dominates. Here, w is the rotation angular velocity of the sphere. The components perpendicular to the sphere motion direction of the hydrodynamic force and surface tension force are F_{hv} and F_{sv}, respectively. The force due to the Magnus effect caused by the sphere rotation is F_l.

torque, which makes the sphere rotate clockwise (speed w), producing a downward force F_l perpendicular to the motion direction caused by the Magnus effect, as sketched in figure 6(a). Therefore, the sphere trajectory is first deflected in the downward direction after oblique impact. Then, F_h decreases quickly after the early sinking stage, while the force due to surface tension F_s increases and becomes the dominant force at the late sinking stage. Owing to the upward deflection of the TPCL plane, F_s has an upward component F_{sv} perpendicular to the motion direction, which gradually exceeds the sum of F_l and F_{hv} at the late sinking stage, as sketched in figure 6(b), thus causing the sphere trajectory to begin to deflect in the upward direction. At the reverting stage, F_{sv} increases further and tends to be vertical because the TPCL plane tends to be horizontal, while F_h becomes extremely small due to the small sphere velocity, as sketched in figure 6(c). This causes the sphere's vertical velocity to decay rapidly and the horizontal velocity to decay slowly. Accordingly, the sphere moves slowly in the horizontal direction. Since the non-axisymmetry of sphere wetting increases with decreasing α, the deviation of the sphere trajectory becomes larger when the impact angle decreases.

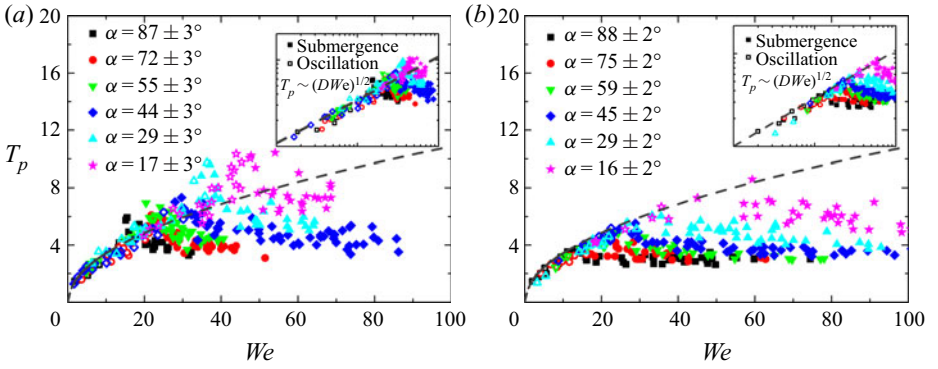

FIGURE 7. The dependences of the dimensionless penetration time T_p $(= t_p u_0/d_p)$ of the microsphere on *We* after impacting on the surfaces of (*a*) water and (*b*) propanol solution with different impact angles, whereby the solid and hollow points represent the submergence and oscillation modes, respectively. The inset panel plots the data in the log–log scale with the same coordinate ranges. The maximum absolute and relative measurement errors of T_p are 0.92 and 19 %, respectively.

3.3. *Penetration time and penetration depth*

The impact processes at the impact angles of near 90°, 75°, 60°, 45°, 30° and 15°, are chosen to give scaling arguments on the penetration time t_p and the penetration depth h_p. The dependence of the dimensionless penetration time T_p $(= t_p u_0/d_p)$ of the microsphere on *We* after impacting on the surfaces of water and propanol solution with different α values is shown in figure 7(*a*,*b*). For oscillating spheres, T_p is independent of α and increases as a function of *We* with a slope of 1/2 in the log–log scale. Since the oscillating spheres have a small *We*, this relationship may be understood by considering the balance between momentum change of the sphere and the surface tension acting on it (Chen *et al.* 2012; Zhu *et al.* 2019), i.e. $m_p(\mathrm{d}u/\mathrm{d}t) = \pi d_p \sigma \sin\phi \sin(\theta + \phi)$. We can scale the momentum term as $\rho_p d_p^3 (d_p/t_p^2)$ and set the surface tension proportional to σd_p, which makes the penetration time follow a characteristic time, i.e. $t_p \sim (\rho_p d_p^3/\sigma)^{1/2}$. Thus, we can find that $T_p \sim (DWe)^{1/2} (D = 1.18$ in our experiment). The simulations conducted by Chen *et al.* (2018) on the impact of millimetre-sized spheres with $Bo = 0.48$ elicited the characteristic penetration time of $t_p \sim (\sigma/(\rho_l g^3))^{1/4} \sim d_p/u_0 We^{1/2} Bo^{-3/4}$, which corresponds to the time taken for a capillary–gravity wave to travel the capillary length $l_c \sim (\sigma/(\rho_l g))^{1/2}$. This expression was also suggested to characterize the pinch-off time of millimetre-sized spheres (Lee & Kim 2008). Our study indicates that the effect of gravity on the evolution of the gas–liquid interface can be neglected during the impact of a microsphere with $Bo \ll 1$, which makes t_p independent of *Bo*. For a submerging sphere, $T_p \approx (s_p/d_p)/(u_a/u_0)$ where $u_a \approx (u_0 + u_p)/2$ is the average velocity of the sphere during the sinking stage. Since the increase in *We* causes a larger u_p and thus results in a larger u_a, T_p decreases with the increase in *We*. This decreasing trend of T_p slows down with increasing *We*, and T_p tends to be constant when *We* is much larger than the critical Weber number for the sphere to submerge. This is because when *We* is large enough, the hydrodynamic force is totally responsible for the energy loss of the sphere, and u_a becomes constant since the decay ratios of the kinetic energies (velocity) of the spheres during the slamming stage have little difference at different *We* values. The increase in α makes T_p decrease due to a decreasing s_p.

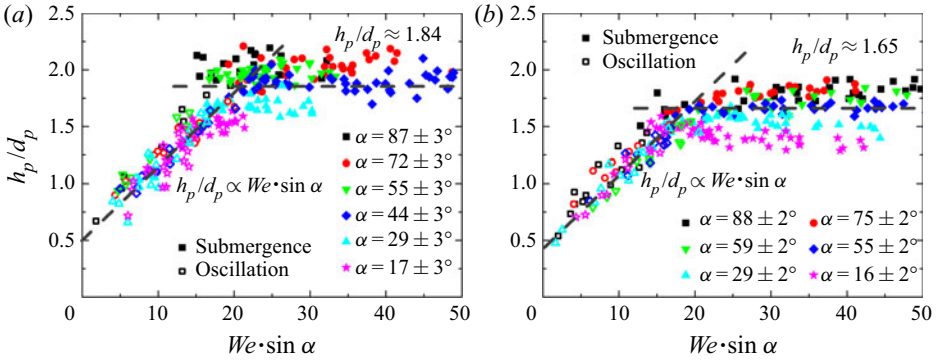

FIGURE 8. Variations of the dimensionless penetration depth h_p/d_p of the microsphere with $We \cdot \sin\alpha$ after impacting on the surfaces of (*a*) water and (*b*) propanol solution with different impact angles, whereby the solid and hollow points represent the submergence and oscillation modes, respectively. The maximum absolute and relative measurement errors of h_p/d_p are 0.22 and 14 %, respectively.

The dependences of the dimensionless penetration depth h_p/d_p of the microsphere with $We \cdot \sin\alpha$ after impacting on the surfaces of water and propanol solution are given in figure 8(*a*,*b*), respectively. It shows that the penetration depth of oscillating spheres keeps to the relationship of $h_p/d_p \propto We \cdot \sin\alpha$. Given that the deviation of the sphere trajectory from its impact direction is typically small, we can find that $s_p \sim h_p/\sin\alpha$. Based on this, we can deduce that $s_p/d_p \propto We$. The same relationship was also found in the numerical studies on the vertical impact of millimetre-sized spheres by Kintea *et al.* (2016) and Chen *et al.* (2018). Since the decay ratios of the kinetic energies of the spheres during the slamming stage have little difference regarding the impacts at different α and We values, the remaining kinetic energy after the slamming stage is consumed mostly by the work expended by the surface tension given that u_p of an oscillating sphere is relatively very small. Accordingly, $\sigma d_p s_p \propto \rho_s d_p^3 u_0^2$, from which the relationship between s_p/d_p and We listed above can be deduced. For submerging spheres, h_p/d_p is maintained almost constant and does not change as a function of We at the same α. The penetration depth of submerging spheres is determined by the evolution of the cavity (Aristoff & Bush 2009). Given the similarity of the TPCL motions of submerging spheres in figure 5(*a*), it can be inferred that the evolutions of the liquid surface after the impact of microspheres with the same impact angle at a certain range of We are self-similar. It seems that the cavity cannot be maintained stable owing to the large curvature near the TPCL when the sphere reaches a certain depth, resulting in the pinch-off of the cavity and the submergence of microsphere (Aristoff & Bush 2009). Thus, a microsphere submerges at a certain penetration depth (Vella & Li 2010), while a millimetre-sized sphere submerges at a certain time (Lee & Kim 2008). Furthermore, the change of h_p/d_p of the submerging sphere with α is small when α is large, while it decreases when $\alpha \leq 45°$. The average h_p/d_p of an oblique submergence mode with $\alpha = 17 \pm 3°$ is approximately 75 % of that of a vertical submergence mode in figure 8(*a*). For the submerging microspheres after impacting on the surfaces of water and propanol solution, h_p/d_p is approximately 1.84 and 1.65, respectively, which is larger than that of a millimetre-sized sphere reported by Chen *et al.* (2018).

3.4. *Criterion for different impact modes*

According to the theoretical prediction by Johnson & Reid (1975), a large PMMA sphere will bounce off the liquid surface when the impact angle is smaller than $18°/D^{1/2} =$

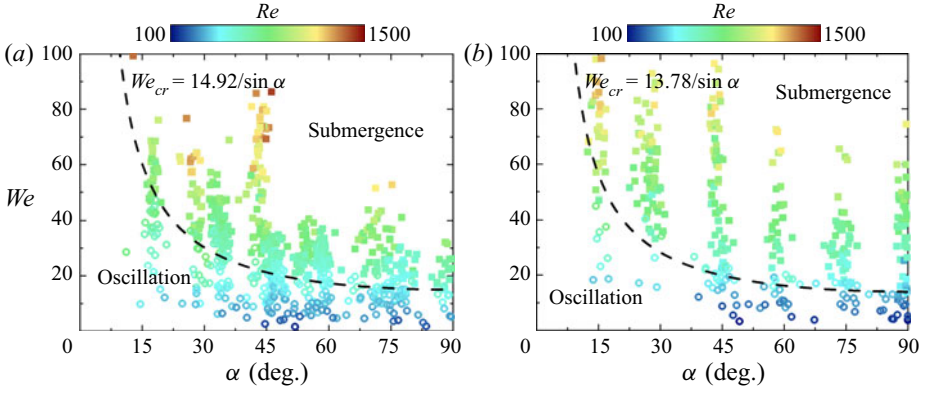

FIGURE 9. Phase diagrams of oblique impact of PMMA microspheres on the surfaces of (*a*) water and (*b*) propanol solution with respect to *We* and α coloured based on *Re*, where the solid squares and hollow circles represent the submergence and oscillation modes, respectively. The maximum absolute and relative measurement errors of *We* are 7.8 and 23 %, respectively, and the maximum absolute and relative measurement errors of α are 4.3° and 8.3 %, respectively. The black dashed lines in (*a*) and (*b*) correspond to the predictions of (3.5) when We_{cr_n} equals to 14.92 and 13.78, respectively.

16.6°. However, the PMMA microspheres did not rebound in our experiment, due to the difference of dominant impact forces between the microspheres (surface tension and hydrodynamic force) and large spheres (gravity and fluid force). Figures 9(*a*) and 9(*b*) show the phase diagrams with respect to *We* and α for the oblique impact of microspheres on the surfaces of water and propanol solution, respectively. There is a clear boundary between the observed two impact modes of submergence and oscillation, which represents the variation of the critical Weber number We_{cr}. Correspondingly, the submerging process near this boundary is referred to as the critical sinking process. The phase diagram shows that We_{cr} decreases as α increases. Herein, we establish a scaling model based on the energy balance during the critical sinking process to derive a criterion which can distinguish different impact modes.

As mentioned above, the gravity and buoyancy can be neglected compared to the hydrodynamic force and surface tension during impact because $Bo \ll 1$ for a microsphere. For the critical sinking process, the kinetic energy of the sphere can be considered to be zero when it submerges. Thus, the initial kinetic energy of the sphere is consumed by the work expended by the hydrodynamic force F_h and the force due to surface tension F_s during the sinking stage.

Here, F_h mainly works at the slamming stage and can be expressed as $F_h = \frac{1}{2}C_h(\pi/4)d_p^2\rho_l u^2$. Shiffman & Spencerd (1945*a*,*b*) theoretically analysed the impact forces on a sphere at the initial stage of the impact, and provided the expression of the resistance coefficient C_h. Subsequent experimental and theoretical research studies indicated that the fluid flow around the sphere with $Re > 10^2$ at the slamming stage could be assumed as a potential flow, and C_h can be considered as a single variable function of h_p (as well as ϕ) (Miloh 1991; Moghisi & Squire 1981). Additionally, it was considered that the momentum loss ratio of the sphere at the slamming stage was unrelated to *We* (Shepard & Abraham 2014). In consideration of the submergence processes evaluated by this study, the evolutions of ϕ with s/s_p were almost the same. Thus, it can be assumed that the momentum (kinetic energy) losses of the sphere at the slamming stage have little

difference regarding the submergence processes at different α and We values, as shown in figure 4(c). Therefore, the work expended by F_h during the sinking process was evaluated according to $W_h \sim a(\pi/8)\rho_l d_p^3 u_0^2$, where a is a constant.

The force due to surface tension can be calculated with $F_s = \pi d_p \sigma \sin\phi \sin(\theta + \phi)$, and the work expended by F_s can be expressed as

$$W_s = \int_0^{s_p} \pi d_p \sigma \sin\phi \sin(\theta + \phi) \cos\left(\frac{\pi}{2} - \alpha_u - \alpha_T\right) \mathrm{d}s, \tag{3.1}$$

where $\pi/2 - \alpha_u - \alpha_T$ is the angle between the opposite direction of F_s and the direction of u. Here, F_s mainly works at the late stage of the critical sinking, and it can be concluded from the experimental data that $\pi/2 - \alpha_u - \alpha_T$ is basically less than 35° at the late stage of the sinking process, which means that $\cos(\pi/2 - \alpha_u - \alpha_T)$ is basically larger than 0.82 at different impact angles. Here we assume $\cos(\pi/2 - \alpha_u - \alpha_T) \approx 1$ for simplification and (3.1) can be reduced as

$$W_s \approx \pi d_p \sigma s_p \int_0^1 \sin\phi \sin(\theta + \phi)\, \mathrm{d}\left(\frac{s}{s_p}\right). \tag{3.2}$$

If we let $b = \int_0^1 \sin\phi \sin(\theta + \phi)\, \mathrm{d}(s/s_p)$, then $W_s \sim b\pi d_p \sigma s_p$. As figure 5($a$) shows, the evolution of ϕ as a function of s/s_p is almost the same for all of the submergence processes, which indicates that b can be considered as a constant in this study. Research on the vertical impact of microspheres (Ji *et al.* 2019) show that b is only related to θ. Thus, the energy balance of the critical sinking process yields

$$\frac{\pi}{12}\rho_s d_p^3 u_0^2 \sim a\frac{\pi}{8}\rho_l d_p^3 u_0^2 + b\pi d_p \sigma s_p. \tag{3.3}$$

Since $s_p \sim h_p/\sin\alpha$, we obtain

$$We_{cr} \sim \frac{24 b h_p/d_p}{(2D - 3a)\sin\alpha}. \tag{3.4}$$

For submerging spheres, we can know from figure 8 that the difference between the h_p/d_p of the impact processes at different α values is small. Thus, (3.4) reduces to the critical sinking criterion for the vertical impact of microspheres when $\alpha = 90^\circ$, and it can be expressed as

$$We_{cr} \sim \frac{We_{cr\_n}}{\sin\alpha}, \tag{3.5}$$

where We_{cr_n} is the critical Weber number for the vertical impact of microspheres, which can be determined by experiment or the criterion proposed by our previous study (Ji *et al.* 2019). The formula shows that We_{cr} for the oblique impact of the microsphere is approximately $1/\sin\alpha$ times that for the vertical impact, which is mainly owing to the increasing work expended by the surface tension force (as well as the surface energy changes of the system) during the sphere's oblique impact process. By calculating the average of the maximum We of oscillating spheres and the minimum We of submerging spheres with $\alpha = 88 \pm 2^\circ$, it can be found that We_{cr_n} equals 14.92 ± 0.62 and 13.78 ± 0.33 for the impacts on the surfaces of water and propanol solution, respectively. Correspondingly, $We_{cr} = 14.92/\sin\alpha$ and $We_{cr} = 13.78/\sin\alpha$ for the impacts on these two liquids surface, respectively, as shown by the dashed lines in figure 9(a,b). Although

Re varies from 115 to 1408 in our experiment, (3.5) can accurately distinguish the two observed impact modes, thus confirming that *Re* has a small effect on the impact process when *Re* is large. When α is small (e.g. $\sim 15^\circ$ in figure 9), the obvious decrease in the penetration depth and increase in the deviation of TPCL plane from the velocity direction will increase the prediction error of (3.5). The detailed sphere dynamics after impacting on the liquid surface with a very small impact angle still remains to be revealed.

4. Conclusions

We investigated the oblique impact of microspheres on the liquid surface experimentally by high-speed microphotography for the first time. The sphere motion and gas–liquid interface evolution were observed, and the effect of the impact angle α on the impact behaviours was studied. Compared with the vertical impact, the sphere rotated during its oblique impact process, and its trajectory deviated downward first and then upward, while the non-axisymmetric liquid surface distortion experienced an evolution from half-cavity to full-cavity. The TPCL motion during impact was also analysed. Findings indicated that the sphere's non-axisymmetric wetting along the motion direction provided an eccentric force deviating from the motion direction, which drove the sphere rotation and deflected the sphere trajectory. The deviation of the sphere trajectory and non-axisymmetry of the liquid surface distortion became more obvious with the decrease of α. The microspheres exhibited two impact modes of oscillation and submergence successively with the increase in α or *We*. Scaling arguments showed that: (i) for the oscillating spheres, the penetration time and penetration depth adhered to $t_p \sim d_p/u_0 We^{1/2}$ and $h_p \sim d_p We \cdot \sin\alpha$, respectively; (ii) for the submerging spheres, the penetration time decreased when α increased, and decreased first and then tended to be constant with the increase in *We*, while the penetration depth decreased slightly when α decreased and was unaffected by *We*. Energy balance analyses showed that the decrease in α resulted in increasing work done by surface tension during the sinking stage, which made the critical *We* increase. The proposed criterion used to distinguish different impact modes indicated that the critical *We* for the oblique impact of the microsphere was $1/\sin\alpha$ times that for vertical impact, and was in good agreement with the experimental results. These will be helpful for the understanding of the related natural phenomenon and for providing guidance to related industrial processes. A full three-dimensional photographic observation will extend the findings of this work, and detailed simulations can elicit more insights on the dynamics of sphere rotation and trajectory deviation during the sphere's oblique impact process at very small impact angles.

Acknowledgements

This work was supported by funds from the National Key Research and Development Program of China (2017YFC0210704) and the National Natural Science Foundation of China (51576109).

Declaration of interests

The authors report no conflict of interest.

Supplementary movies

Supplementary movies are available at https://doi.org/10.1017/jfm.2020.511.

REFERENCES

ARISTOFF, J. M. & BUSH, J. W. 2009 Water entry of small hydrophobic spheres. *J. Fluid Mech.* **619**, 45–78.

ARISTOFF, J. M., TRUSCOTT, T. T., TECHET, A. H. & BUSH, J. W. 2010 The water entry of decelerating spheres. *Phys. Fluids* **22**, 70–340.

BAE, S. Y., JUNG, C. H. & KIM, Y. P. 2010 Derivation and verification of an aerosol dynamics expression for the below-cloud scavenging process using the moment method. *J. Aerosol Sci.* **41**, 266–280.

BERGMANN, R., VAN DER MEER, D., GEKLE, S., VAN DER BOS, A. & LOHSE, D. 2009 Controlled impact of a disk on a water surface: cavity dynamics. *J. Fluid Mech.* **633**, 381–409.

BODILY, K. G. 2013 The water entry of slender axisymmetric bodies: forces, trajectories and acoustics. MS thesis, Brigham Young University, Provo, UT.

BUSH, J. W. & HU, D. L. 2006 Walking on water: biolocomotion at the interface. *Annu. Rev. Fluid Mech.* **38**, 339–369.

CHEN, L., HEIM, L., GOLOVKO, D. S. & BONACCURSO, E. 2012 Snap-in dynamics of single particles to water drops. *Appl. Phys. Lett.* **101** (3), 031601.

CHEN, H., LIU, H., LU, X. & DING, H. 2018 Entrapping an impacting particle at a liquid–gas interface. *J. Fluid Mech.* **841**, 1073–1084.

CLANET, C., HERSEN, F. & BOCQUET, L. 2004 Secrets of successful stone-skipping. *Nature* **427**, 29–29.

DING, H., CHEN, B. Q., LIU, H. R., ZHANG, C. Y., GAO, P. & LU, X. Y. 2015 On the contact-line pinning in cavity formation during solid–liquid impact. *J. Fluid Mech.* **783**, 504–525.

DUEZ, C., YBERT, C., CLANET, C. & BOCQUET, L. 2007 Making a splash with water repellency. *Nat. Phys.* **3**, 180–183.

GEKLE, S., GORDILLO, J. M., VAN DER MEER, D. & LOHSE, D. 2009 High-speed jet formation after solid object impact. *Phys. Rev. Lett.* **102**, 034502.

GRUMSTRUP, T., KELLER, J. B. & BELMONTE, A. 2007 Cavity ripples observed during the impact of solid objects into liquids. *Phys. Rev. Lett.* **99**, 114502.

HRUBES, J. D. 2001 High-speed imaging of supercavitating underwater projectiles. *Exp. Fluids* **30**, 57–64.

HU, D. L., CHAN, B. & BUSH, J. W. 2003 The hydrodynamics of water strider locomotion. *Nature* **424**, 663–666.

JAWOREK, A., BALACHANDRAN, W., KRUPA, A., KULON, J. & LACKOWSKI, M. 2006 Wet electroscrubbers for state of the art gas cleaning. *Environ. Sci. Technol.* **40**, 6197–6207.

JI, B., SONG, Q., WANG, A. & YAO, Q. 2019 Critical sinking of hydrophobic micron particles. *Chem. Eng. Sci.* **207**, 17–29.

JI, B., SONG, Q. & YAO, Q. 2017 Numerical study of hydrophobic micron particle's impaction on liquid surface. *Phys. Fluids* **29**, 3627–3628.

JI, B., SONG, Q. & YAO, Q. 2018 Limit for small spheres to float by dynamic analysis. *Langmuir* **34**, 10163–10168.

JOHNSON, W. 1998 The ricochet of spinning and non-spinning spherical projectiles, mainly from water. Part II: An outline of theory and warlike applications. *Intl J. Impact Engng* **21**, 25–34.

JOHNSON, W. & REID, S. R. 1975 Ricochet of spheres off water. *J. Mech. Engng Sci.* **17**, 71–81.

KAPTAY, G. 1996 Interfacial phenomena during melt processing of ceramic particle-reinforced metal matrix composites. Part II: Interfacial force between a spherical particle and an approaching solid/liquid interface. *Mater. Sci. Forum* **215–216**, 467–474.

KIM, S. J., FEZZAA, K., AN, J., SUN, T. & JUNG, S. 2017 Capillary spreading of contact line over a sinking sphere. *Appl. Phys. Lett.* **111**, 134102.

KINTEA, D. M., BREITENBACH, J., GURUMURTHY, V. T., ROISMAN, I. V. & TROPEA, C. 2016 On the influence of surface tension during the impact of particles on a liquid-gaseous interface. *Phys. Fluids* **28**, 012108.

LEE, D. G. & KIM, H. Y. 2008 Impact of a superhydrophobic sphere onto water. *Langmuir* **24**, 142–145.

LIU, D., HE, Q. & EVANS, G. M. 2010 Penetration behaviour of individual hydrophilic particle at a gas–liquid interface. *Adv. Powder Technol.* **21**, 401–411.

MILOH, T. 1991 On the oblique water-entry problem of a rigid sphere. *J. Engng Maths* **25**, 77–92.

MITRA, S., DOROODCHI, E., PAREEK, V., JOSHI, J. & EVANS, G. 2015 Collision behaviour of a smaller particle into a larger stationary droplet. *Adv. Powder Technol.* **26**, 280–295.

MOGHISI, M. & SQUIRE, P. T. 1981 An experimental investigation of the initial force of impact on a sphere striking a liquid surface. *J. Fluid Mech.* **108**, 133–146.

ROSELLINI, L., HERSEN, F., CLANET, C. & BOCQUET, L. 2005 Skipping stones. *J. Fluid Mech.* **543**, 137–146.

SEDDON, C. & MOATAMEDI, M. 2006 Review of water entry with applications to aerospace structures. *Intl J. Impact Engng* **32**, 1045–1067.

SHEPARD, T. & ABRAHAM, J 2014 Effect of impact velocity and mass ratio during vertical sphere water entry. *Dev. Appl. Oceanic Engng* **3**, 55–62.

SHIFFMAN, M. & SPENCERD, C. 1945*a* The force of impact on a sphere striking a water surface. *AMP Tech. Rep.* 42, lR. AMG-NYU No. 105.

SHIFFMAN, M. & SPENCERD, C. 1945*b* The force of impact on a sphere striking a water surface. *AMP Tech. Rep.* 42, 2R. AMG-NYU No. 133.

SPEIRS, N. B., MANSOOR, M. M., BELDEN, J. & TRUSCOTT, T. T. 2019 Water entry of spheres with various contact angles. *J. Fluid Mech.* **862**, R3.

TRUSCOTT, T. T., EPPS, B. P. & BELDEN, J. 2013 Water entry of projectiles. *Annu. Rev. Fluid Mech.* **46**, 355–378.

VELLA, D. & LI, J. 2010 The impulsive motion of a small cylinder at an interface. *Phys. Fluids* **22**, 289.

WANG, A., SONG, Q., JI, B. & YAO, Q. 2017 In-situ observation of hydrophobic micron particle impaction on liquid surface. *Powder Technol.* **311**, 408–415.

WON, Y. S., CHUNG, D. K. & MILLS, A. F. 1981 Density, viscosity, surface tension, and carbon dioxide solubility and diffusivity of methanol, ethanol, aqueous propanol, and aqueous ethylene glycol at 25 °C. *J. Chem. Engng Data* **26** (2), 140–141.

WU, N. 2013 Experimental methodology investigation of pulverized coal combustion in counterflow flames. PhD thesis, Tsinghua University.

ZHU, S. J., LIU, R. Z., WANG, T., NIU, Y. J., LU, H. F. & CHEN, X. L. 2019 Penetration time of hydrophilic micron particles impacting into an unconfined planar gas–liquid interface. *Chem. Engng Sci.* **193**, 282–297.